

# Evidence for energy injection and a fine-tuned central engine at optical wavelengths in GRB 070419A

A. Melandri<sup>1\*</sup>, C. Guidorzi<sup>2,3,1</sup>, S. Kobayashi<sup>1</sup>, D. Bersier<sup>1</sup>, C. G. Mundell<sup>1</sup>,  
P. Milne<sup>4</sup>, A. Pozanenko<sup>5</sup>, W. Li<sup>6</sup>, A. V. Filippenko<sup>6</sup>, Y. Urata<sup>7</sup>, M. Ibrahimov<sup>8</sup>,  
I. A. Steele<sup>1</sup>, A. Gomboc<sup>9</sup>, R. J. Smith<sup>1</sup>, N. R. Tanvir<sup>10</sup>, E. Rol<sup>10</sup>

<sup>1</sup>*Astrophysics Research Institute, Liverpool John Moores University, Twelve Quays House, Egerton Wharf, Birkenhead, CH41 1LD, UK.*

<sup>2</sup>*Dipartimento di Fisica, Università di Ferrara, via Saragat 1, I-44100 Ferrara, Italy.*

<sup>3</sup>*INAF-Osservatorio Astronomico di Brera, via Bianchi 46, I-23807 Merate (LC), Italy.*

<sup>4</sup>*Steward Observatory, University of Arizona, 933 North Cherry Avenue, Tucson, AZ 85721, USA.*

<sup>5</sup>*Space Research Institute (IKI), 84/32 Profyuznaya Str, Moscow 117997, Russia.*

<sup>6</sup>*Department of Astronomy, University of California, Berkeley, CA 94720-3411, USA.*

<sup>7</sup>*Department of Physics, Saitama University, Saitama 338-8570, Japan.*

<sup>8</sup>*Ulugh Beg Astronomical Institute, Tashkent 700052, Uzbekistan.*

<sup>9</sup>*Faculty of Mathematics and Physics, University of Ljubljana, Jadranska 19, SI-1000 Ljubljana, Slovenia.*

<sup>10</sup>*Department of Physics and Astronomy, University of Leicester, University Road, Leicester LE1 7RH, UK.*

## ABSTRACT

We present a comprehensive multiwavelength temporal and spectral analysis of the FRED GRB 070419A. The early-time emission in the  $\gamma$ -ray and X-ray bands can be explained by a central engine active for at least 250 s, while at late times the X-ray light curve displays a simple power-law decay. In contrast, the observed behaviour in the optical band is complex (from  $10^2$  up to  $10^6$  s). We investigate the light curve behaviour in the context of the standard forward/reverse shock model; associating the peak in the optical light curve at  $\sim 450$  s with the fireball deceleration time results in a Lorentz factor  $\Gamma \approx 350$  at this time. In contrast, the shallow optical decay between 450 and 1500 s remains problematic, requiring a reverse shock component whose typical frequency is above the optical band at the optical peak time for it to be explained within the standard model. This predicts an increasing flux density for the forward shock component until  $t \sim 4 \times 10^6$  s, inconsistent with the observed decay of the optical emission from  $t \sim 10^4$  s. A highly magnetized fireball is also ruled out due to unrealistic microphysic parameters and predicted light curve behaviour that is not observed. We conclude that a long-lived central engine with a finely tuned energy injection rate and a sudden cessation of the injection is required to create the observed light curves - consistent with the same conditions that are invoked to explain the plateau phase of canonical X-ray light curves of GRBs.

**Key words:** gamma rays: bursts

## 1 INTRODUCTION

The temporal shape of the prompt emission of gamma-ray bursts (GRBs) can show a variety of profiles: from narrow and symmetric to wide and asymmetric pulses. In some cases a less energetic precursor is also detected, and in other cases a few overlapping pulses can take place for the entire duration of the  $\gamma$ -ray emission. It is true that many of those pulses (overlapping or single) detected for long-duration GRBs can be described by the superposition of “fast rise exponential decay” (FRED) profiles, one for each pulse. More-

over, several GRBs display only a single-shot FRED-like emission over the background in the  $\gamma$ -ray passband, that can be easily described by a simple Norris exponential model (Norris et al. 1996). In the context of the standard fireball model (Rees & Mészáros 1992) one may expect such GRBs to exhibit comparably simple behaviour in their afterglows at other wavelengths, and therefore be ideal testbeds for the model. For full temporal and spectral coverage, the predicted properties of the multiwavelength light curves have well-predicted shapes, depending on the relative contribution of the different components.

In the X-ray band the temporal decay of many GRBs observed by *Swift* is well described by a canonical “steep-shallow-steep” de-

\* E-mail: axm@astro.livjm.ac.uk

cay (Tagliaferri et al. 2005; Nousek et al. 2006; Zhang et al. 2006), with superposed flares observed in  $\sim 50\%$  of bursts (O’Brien et al. 2006; Chincarini et al. 2007; Falcone et al. 2007). The initial steep decay is interpreted as the result of the high-latitude emission or as the contribution of the reverse-shock emission (e.g., Panaitescu & Kumar; Zhang et al. 2006), the shallow phase is consistent with long-lasting central energy activity (Zhang et al. 2006), and the late steep decay is evidence of decaying forward-shock emission, (i.e., the standard X-ray afterglow phase).

In the optical band, observed light curves are expected to show a variety of shapes depending on the relative contribution of the forward- and reverse-shock emission (Kobayashi & Zhang 2003; Zhang, Kobayashi & Mészáros 2003) and the starting time of the observations. In particular, if the optical observations start when the reverse-shock contribution still dominates or when the central engine is still active, the detected temporal decay deviates from a simple power law (see fig. 1 in Melandri et al. 2008). Melandri et al. (2008) investigated the behaviour of the early decay phase in the optical and X-ray bands for 24 GRBs and classified them into four self-consistent groups based on the relative shapes observed in the two bands. Although 14 of the GRBs were well described by the standard model, the remaining 10 required adaptations such as ambient density gradients or energy injections from long-lived central engines. In some cases, even these modifications were unable to fully explain the light-curve properties.

GRB 070419A was particularly problematic, despite a simple FRED  $\gamma$ -ray profile. In this paper we present a comprehensive multiwavelength temporal and spectral study of GRB 070419A, including published and unpublished data from infrared to  $\gamma$ -ray bands, and use this extensive dataset to challenge the standard model.

Throughout we use the following conventions: the power-law flux density is given as  $F(\nu, t) \propto t^{-\alpha} \nu^{-\beta}$ , where  $\alpha$  is the temporal decay index and  $\beta$  is the spectral slope; we assume a standard cosmology with  $H_0 = 70 \text{ km s}^{-1} \text{ Mpc}^{-1}$ ,  $\Omega_m = 0.3$ , and  $\Omega_\Lambda = 0.7$ ; and all uncertainties are quoted at the  $1\sigma$  confidence level (cl), unless stated otherwise.

## 2 OBSERVATIONS

### 2.1 *Swift*/BAT data

On 2007 April 19 at 09:59:26 UT the Burst Alert Telescope (BAT; Barthelmy et al. 2005) triggered on GRB 070419A (Stamatikos et al. 2007a), a dim long GRB with a duration of  $T_{90} \approx 110$  s. The  $\gamma$ -ray emission observed by BAT is a single-shot FRED light curve, with a total duration of a few hundred seconds. This event displayed an average  $\gamma$ -ray fluence ( $\sim 5 \times 10^{-7} \text{ erg cm}^{-2}$ ) and a peak photon flux lying at the low end of the distribution of *Swift* GRBs (Sakamoto et al. 2008). The redshift of the burst ( $z = 0.97$ , Cenko et al. 2007) resulted in an isotropic energy estimate of  $\sim 1.6 \times 10^{51}$  ergs in the 15–150 keV observed bandpass (Stamatikos et al. 2007c).

### 2.2 *Swift*/XRT data

Follow-up observations of the BAT error circle were performed with the X-ray Telescope (XRT; Burrows et al. 2005) starting about 113 s after the BAT trigger. A bright, uncatalogued, fading source was detected at  $\alpha(\text{J2000}) = 12^{\text{h}}10^{\text{m}}58.80^{\text{s}}$ ,  $\delta(\text{J2000}) = +39^{\circ}55'32.4''$  (Perri et al. 2007) with an uncertainty of  $2.2''$ . The light curve showed a rapid decay at early times followed (after

**Table 1.** Log of the optical observations.

Telescope	Filters	$\Delta t_{\text{start}}$ (min)	$\Delta t_{\text{end}}$ (min)	Reference
Super-LOTIS	<i>R</i>	3.43	35.46	This work
KAIT	<i>VRl</i>	5.24	57.66	This work
P60	<i>Ri'</i>	5.87	92.35	Cenko et al. (2008)
Kuiper	<i>VR</i>	27.68	97.68	This work
FTN	<i>BRi'</i>	39.43	101.46	This work
Kiso	<i>BR</i>	51.05	112.24	This work
Lulin	<i>R</i>	112.75	236.32	This work
Maidanak	<i>R</i>	352.80	352.80	This work
KPNO 4-m	<i>R</i>	1036.97	1036.97	This work
LBT	<i>r'</i>	5328.00	44352.00	Dai et al. (2007)

$\Delta t_{\text{start}}$  and  $\Delta t_{\text{end}}$  refer to the first and last photometric measurement acquired with the corresponding telescope. A complete list of all the photometric points presented on this work is reported in Table 2.

$10^3$  s) by a power-law decline with  $\alpha = 1.2 \pm 0.2$ . The X-ray spectrum is well fitted by an absorbed power law with a photon index  $\Gamma_X = 2.46 \pm 0.09$  and  $N_H = (1.9 \pm 0.2) \times 10^{21} \text{ cm}^{-2}$  (Stamatikos et al. 2007c).

### 2.3 Optical data

The afterglow of GRB 070419A was followed in the optical band from about 3 min and continued up to  $\sim 18$  hr after the burst event. Late-time observations were acquired with the 8.4-m Large Binocular Telescope (LBT) in the SDSS-*r* filter and showed a bump in the light curve (Dai et al. 2007), compatible with a supernova bump (see Section 4.3 for a more detailed discussion of the possible supernova contribution). A log of the observations is given in Table 1, where we report the starting and ending time of the observations with each facility.

We collected, cross-calibrated, and analysed all the available optical data acquired by ground-based telescopes for this event. We calibrated the optical data using a common set of selected catalogued stars present in the field of view. SDSS pre-burst observation (Cool et al. 2007) has been used for *r'* and *i'* filters, USNO-B1 *R2* and *B2* magnitudes for *R* and *B* filters respectively, and Nomad *V* magnitudes for the *V* filter. LBT *r'* magnitudes are reported in the *R* band applying an average color term of  $\langle R - r' \rangle \approx -0.31$  mag, estimated from several field stars. In the same way, KAIT *I*-band magnitudes are given in the *i'* band assuming an average color term of  $\langle I - i' \rangle \approx -0.93$  mag.

Next, the calibrated magnitudes were corrected for the Galactic absorption along the line of sight ( $E_{B-V} = 0.028$  mag; Schlegel et al. 1998); the estimated extinctions in the different filters are  $A_B = 0.12$  mag,  $A_V = 0.09$  mag,  $A_R = 0.07$  mag, and  $A_{i'} = 0.05$  mag. Corrected magnitudes were then converted into flux densities,  $F_\nu$  (mJy), following Fukugita et al. (1996). Results are summarized in Table 2.

The optical afterglow of GRB 070419A was also detected by the *Swift*/UVOT (Romig et al. 2005). Observations began  $\sim 115$  s after the event. The best position for the optical afterglow is measured in the KAIT images at  $\alpha(\text{J2000}) = 12^{\text{h}}10^{\text{m}}58.82^{\text{s}}$ ,  $\delta(\text{J2000}) = +39^{\circ}55'33.92''$  (Chornock et al. 2007). Deriving accurate photometry of the afterglow was difficult, due to the presence of a diffraction spike from a mag 7 star in the field of view. A clear detection was possible in the *V* band, while only a  $3\sigma$  upper limits was estimated for the *B* and *U* filters (Stamatikos et al. 2007c). UVOT-*V*

**Table 2.** Optical and infrared calibrated magnitudes for the afterglow of GRB 070419A.

Filter	Telescope	$\Delta t$ (min)	Exp. Time (min)	Magnitude	$F_\nu$ (mJy)	Filter	Telescope	$\Delta t$ (min)	Exp. Time (min)	Magnitude	$F_\nu$ (mJy)
R	S-Lotis	3.436	2.5	19.60 ± 0.21	0.0476 ± 0.0092	B	FTN	47.97	1.67	20.86 ± 0.30	0.0205 ± 0.0057
R	S-Lotis	3.925	2.0	19.75 ± 0.23	0.0415 ± 0.0088	B	FTN	56.25	2.0	21.62 ± 0.35	0.0102 ± 0.0033
R	S-Lotis	7.597	1.0	18.45 ± 0.12	0.1375 ± 0.0152	B	FTN	65.13	3.0	21.69 ± 0.29	0.0095 ± 0.0025
R	S-Lotis	8.718	1.0	18.65 ± 0.12	0.1143 ± 0.0126	B	FTN	80.09	5.0	21.90 ± 0.23	0.0078 ± 0.0016
R	S-Lotis	10.889	2.0	18.76 ± 0.11	0.1033 ± 0.0104	B	FTN	96.90	4.0	22.17 ± 0.30	0.0061 ± 0.0017
R	S-Lotis	13.062	2.0	18.84 ± 0.11	0.0959 ± 0.0097	B	Kiso	58.78	5.0	21.80 ± 0.28	0.0086 ± 0.0022
R	S-Lotis	15.968	4.0	18.90 ± 0.08	0.0908 ± 0.0067	B	Kiso	74.18	5.0	21.50 ± 0.24	0.0114 ± 0.0025
R	S-Lotis	20.428	4.0	19.02 ± 0.08	0.0813 ± 0.0060	B	Kiso	89.41	5.0	22.20 ± 0.48	0.0059 ± 0.0027
R	S-Lotis	24.886	4.0	19.14 ± 0.14	0.0728 ± 0.0094	B	Kiso	104.60	5.0	22.49 ± 0.48	0.0045 ± 0.0021
R	S-Lotis	29.677	5.0	19.27 ± 0.10	0.0646 ± 0.0059						
R	S-Lotis	35.468	5.0	19.58 ± 0.13	0.0485 ± 0.0058	V	KAIT	5.245	2.0	19.811 ± 0.55	0.0470 ± 0.0248
R	KAIT	3.665	0.333	20.45 ± 0.88	0.0218 ± 0.0196	V	Kuiper	36.553	1.0	19.961 ± 0.11	0.0410 ± 0.0041
R	KAIT	6.208	0.75	19.19 ± 0.17	0.0695 ± 0.0109	V	Kuiper	38.388	1.0	19.857 ± 0.11	0.0451 ± 0.0045
R	KAIT	9.733	1.0	18.59 ± 0.08	0.1208 ± 0.0089	V	Kuiper	40.122	1.0	20.112 ± 0.12	0.0356 ± 0.0039
R	KAIT	21.65	1.0	19.07 ± 0.14	0.0776 ± 0.0100	V	Kuiper	41.858	1.0	20.144 ± 0.12	0.0346 ± 0.0038
R	KAIT	24.00	1.0	19.29 ± 0.18	0.0634 ± 0.0105	V	Kuiper	43.597	1.0	20.237 ± 0.13	0.0318 ± 0.0038
R	KAIT	26.40	1.0	19.26 ± 0.18	0.0652 ± 0.0108	V	Kuiper	45.336	1.0	20.141 ± 0.12	0.0347 ± 0.0038
R	KAIT	30.572	3.0	19.57 ± 0.22	0.0490 ± 0.0099	V	Kuiper	47.075	1.0	19.990 ± 0.11	0.0399 ± 0.0040
R	KAIT	36.483	2.0	19.97 ± 0.25	0.0339 ± 0.0078	V	Kuiper	48.826	1.0	20.009 ± 0.11	0.0392 ± 0.0039
R	KAIT	41.173	5.0	20.15 ± 0.21	0.0287 ± 0.0055	V	Kuiper	50.566	1.0	20.182 ± 0.13	0.0334 ± 0.0040
R	KAIT	47.653	6.0	20.57 ± 0.30	0.0195 ± 0.0054	V	Kuiper	52.315	1.0	19.956 ± 0.11	0.0412 ± 0.0041
R	KAIT	57.661	7.0	20.71 ± 0.33	0.0171 ± 0.0053	V	Kuiper	54.054	1.0	20.502 ± 0.17	0.0249 ± 0.0039
R	Kuiper	27.681	1.0	19.54 ± 0.07	0.0503 ± 0.0032	V	Kuiper	55.790	1.0	20.433 ± 0.16	0.0265 ± 0.0039
R	Kuiper	29.420	1.0	19.50 ± 0.07	0.0522 ± 0.0033	V	Kuiper	57.524	1.0	20.774 ± 0.21	0.0194 ± 0.0037
R	Kuiper	31.148	1.0	19.65 ± 0.08	0.0455 ± 0.0033	V	Kuiper	59.257	1.0	20.387 ± 0.15	0.0277 ± 0.0038
R	Kuiper	32.890	1.0	19.60 ± 0.07	0.0477 ± 0.0030	V	Kuiper	97.687	12.0	21.663 ± 0.30	0.0085 ± 0.0024
R	Kuiper	64.489	4.0	20.81 ± 0.10	0.0156 ± 0.0014						
R	Kuiper	69.23	4.0	20.83 ± 0.10	0.0153 ± 0.0014	I	KAIT	7.695	1.0	19.56 ± 0.45	0.0571 ± 0.0243
R	Kuiper	73.96	4.0	20.95 ± 0.10	0.0137 ± 0.0012	I	KAIT	8.500	1.0	18.84 ± 0.25	0.1109 ± 0.0257
R	Kuiper	78.71	4.0	21.03 ± 0.11	0.0128 ± 0.0012	I	KAIT	11.05	1.0	18.50 ± 0.18	0.1517 ± 0.0252
R	Kuiper	83.46	4.0	21.26 ± 0.18	0.0103 ± 0.0017	I	KAIT	13.40	1.0	18.59 ± 0.22	0.1397 ± 0.0285
R	Kuiper	88.751	4.0	21.13 ± 0.12	0.0116 ± 0.0013	I	KAIT	16.44	2.0	18.75 ± 0.11	0.1205 ± 0.0122
R	FTN	39.430	1.0	20.20 ± 0.24	0.0274 ± 0.0061	I	KAIT	22.32	3.0	18.99 ± 0.12	0.0966 ± 0.0107
R	FTN	47.384	0.5	20.37 ± 0.16	0.0234 ± 0.0034	I	KAIT	31.77	5.0	20.18 ± 0.48	0.0323 ± 0.0147
R	FTN	51.914	1.0	20.40 ± 0.16	0.0228 ± 0.0033	i'	FTN	46.644	0.667	20.73 ± 0.32	0.0194 ± 0.0058
R	FTN	58.809	2.0	20.46 ± 0.12	0.0216 ± 0.0023	i'	FTN	53.698	1.0	20.58 ± 0.17	0.0223 ± 0.0035
R	FTN	68.706	3.0	20.92 ± 0.15	0.0141 ± 0.0019	i'	FTN	60.615	2.0	20.90 ± 0.16	0.0166 ± 0.0024
R	FTN	78.623	2.0	21.10 ± 0.20	0.0119 ± 0.0022	i'	FTN	72.505	3.0	20.96 ± 0.14	0.0157 ± 0.0020
R	FTN	88.642	3.0	21.30 ± 0.21	0.0099 ± 0.0019	i'	FTN	81.405	2.0	20.96 ± 0.16	0.0157 ± 0.0023
R	FTN	101.46	4.0	21.15 ± 0.15	0.0114 ± 0.0015	i'	FTN	92.399	3.0	21.58 ± 0.30	0.0089 ± 0.0024
R	Lulin	112.75	10.0	21.26 ± 0.17	0.0103 ± 0.0016						
R	Lulin	125.31	15.0	21.70 ± 0.14	0.0068 ± 0.0009	J	UKIRT	39.24	3.0	18.27 ± 0.08	0.0802 ± 0.0059
R	Lulin	236.32	30.0	22.43 ± 0.17	0.0035 ± 0.0005	J	UKIRT	48.84	3.0	18.56 ± 0.09	0.0614 ± 0.0051
R	Kiso	51.05	5.0	20.13 ± 0.11	0.0292 ± 0.0029						
R	Kiso	66.65	5.0	20.75 ± 0.20	0.0165 ± 0.0030	H	UKIRT	44.04	3.0	17.83 ± 0.13	0.0766 ± 0.0092
R	Kiso	81.88	5.0	20.90 ± 0.23	0.0144 ± 0.0030						
R	Kiso	112.24	15.0	21.66 ± 0.34	0.0071 ± 0.0022	K	UKIRT	53.76	3.0	17.26 ± 0.18	0.0838 ± 0.0139
R	Maidanak	352.8	55.0	22.45 ± 0.32	0.0034 ± 0.0010	K	UKIRT	99.90	15.0	18.30 ± 0.18	0.0321 ± 0.0053
R	KPNO 4-m	1036.97	5.0	23.37 ± 0.20	0.0014 ± 0.0003						

Magnitudes are not corrected for Galactic absorption. P60 (Cenko et al. 2008) and LBT (Dai et al. 2007) magnitudes are not reported in this table, but they are plotted in Fig. 9. KAIT-*I* magnitudes have been calibrated against SDSS-*i'* catalogued magnitudes. Flux densities ( $F_\nu$ ) have been estimated from extinction-corrected magnitudes.

magnitudes are plotted together with all of the ground-based optical data (Fig. 7 in Section 3.5), but no cross-calibration between UVOT and other optical data was performed. Thus we cannot exclude the presence of a large offset between UVOT magnitudes and calibrated ground-based photometry.

### 3 RESULTS

We have undertaken a complete temporal and spectral analysis of the available *Swift* data. In this section we report the results of our  $\gamma$ -ray/X-ray/optical analysis.

#### 3.1 Gamma rays

##### 3.1.1 Gamma-ray light curve

As observed by BAT, the  $\gamma$ -ray behaviour of GRB 070419A is a single FRED light curve, lasting a few hundreds seconds. It can be easily fit with a Norris simple exponential model (peakedness fixed to 1):

$$\begin{aligned}
 F(t) &= N^{\text{BAT}} \times e^{-|t-t_{\text{peak}}|/t_{\text{rise}}} & t < t_{\text{peak}} \\
 &= N^{\text{BAT}} \times e^{-(t-t_{\text{peak}})/t_{\text{decay}}} & t > t_{\text{peak}}.
 \end{aligned}
 \tag{1}$$

The parameters of the best-fitting are  $t_{\text{peak}}^{\text{BAT}} = 4.4 \pm 3.4$  s,  $t_{\text{rise}}^{\text{BAT}} = 27.3 \pm 5.6$  s, and  $t_{\text{decay}}^{\text{BAT}} = 93.0 \pm 11.0$  s ( $\chi^2/\text{dof}=0.49$ ). The BAT light curve visible in Fig. 1 shows significant emission above the background up to 300 s after the burst onset time. In the same figure

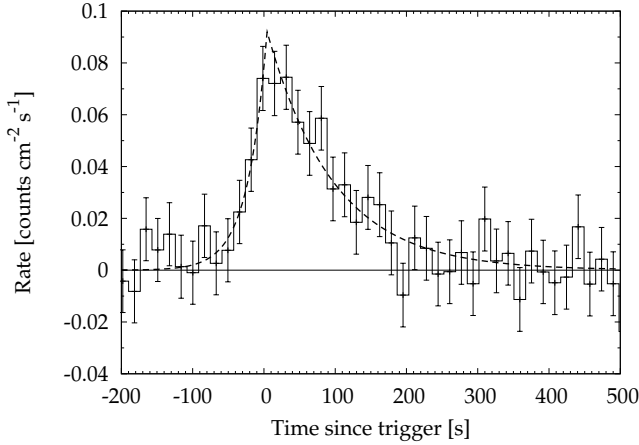


**Figure 1.** The BAT light curve. There is significant emission above the background up to  $t \approx 300$  s. The dashed line represents the best-fitting of the light curve with the Norris profile.

we show the result of the fit of the light curve done in the interval  $-100$  to  $300$  s.

### 3.1.2 Gamma-ray spectral analysis

We independently analysed BAT data with the standard BAT pipeline (Krimm et al. 2004). Using the tool “battblocks” (v1.7) we determined a value of  $T_{90} = 112 \pm 2$  s (going from  $-26$  s to  $+86$  s). Fitting the  $15\text{--}150$  keV spectrum with a single power law, integrated over the  $T_{90}$  interval, gives  $\Gamma_{\gamma} = 2.4 \pm 0.3$ , fluence  $f = 5.1 \pm 0.8 \times 10^{-7}$  erg  $\text{cm}^{-2}$ , and a corresponding peak photon flux of  $0.14 \pm 0.3$  ph  $\text{cm}^{-2} \text{s}^{-1}$ . All of these results are in agreement with the BAT team’s published values (Stamatikos et al. 2007b,c).

## 3.2 X-rays

### 3.2.1 X-ray light curve

From our independent analysis of the XRT data we find that the light curve in the X-ray band can be fitted by an exponential plus power-law model,

$$F(t) = N_{\text{exp}}^{\text{XRT}} \times e^{-(t-t_0)/\tau} + N_{\text{pl}}^{\text{XRT}} \times t^{-\alpha_X}, \quad (2)$$

with best-fitting parameters (uncertainties are 90% cl)  $t_0 = 0.0$  s (fixed, as insensitive parameter),  $\tau = (71.9 \pm 2.4)$  s, and  $\alpha_X = 1.27_{+0.18}^{-0.12}$ . The result of the fit can be seen in Fig. 2, where the two components of the fit are shown separately. These values are in good agreement with those found by Stamatikos et al. (2007c). However, the  $\chi^2$  per degree of freedom (dof) of this fit is not acceptable ( $\chi^2/\text{dof} = 190/127 \approx 1.5$ ).

A more complex model (exponential with peakedness free to vary, plus two power laws) gives a satisfactory result. The justification for a more complex model is the unacceptable  $\chi^2$  of the previous fit, due to bad residuals of the early-time X-ray data. The best-fitting parameters are  $N_{\text{exp}}^{\text{XRT}} = 32.1_{+13.4}^{-7.5}$  counts  $\text{s}^{-1}$ ,  $t_0 = 0.0$  s (fixed),  $\tau = 259_{+13}^{-18}$  s, peakedness =  $5.6_{+2.2}^{-1.6}$ ,  $N_{\text{pl1}}^{\text{XRT}} = 14.96_{+9.53}^{-5.58} \times 10^7$  counts  $\text{s}^{-1}$ ,  $N_{\text{pl2}}^{\text{XRT}} = 1.6 \pm 0.7$  counts  $\text{s}^{-1}$ ,  $\alpha_{X,1} = 3.0 \pm 0.1$ , and  $\alpha_{X,2} = 0.65_{+0.35}^{-0.39}$ . With this more complex model the  $\chi^2$  is now acceptable ( $\chi^2/\text{dof} = 137/124 \approx 1.1$ ). Evidently, the improvement in the total  $\chi^2$  is too large (53) compared with the change in the degrees of freedom (3), when moving from the first to the second

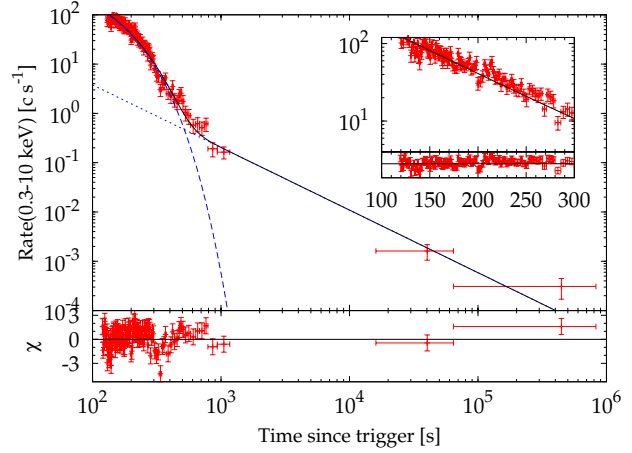


**Figure 2.** The XRT light curve, fitted using the exponential plus single power law model as explained in the text. The two components of the model are shown separately. In the inset the fit of the first 300 s of data with the exponential function is shown together with the residuals of the fit.

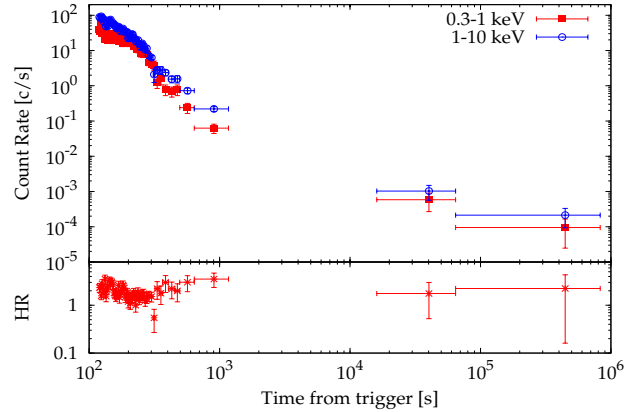


**Figure 3.** Hardness ratio (HR) and X-ray light curve in two different bands. At early times a spectral softening of the emission is visible over the first 200 s of data.

model. The P-value associated with this change in the  $\chi^2$  with 3 dof is  $2 \times 10^{-11}$ , so completely negligible, in agreement with what one would obtain with an F-test. However, it should be noted that the goodness of the fit in this case is related to the sparse data coverage at very late times.

In Fig. 3 the X-ray light curve extracted in two separate bands (0.3–1 keV and 1–10 keV) is shown, together with the hardness ratio (hard/soft, lower panel) in the X-ray band. At early times (between  $\sim 100$  and  $\sim 300$  s) the X-ray emission softened, then hardened up to  $\sim 1000$  s when the hardness ratio became roughly constant up to the end of the observations.

### 3.2.2 X-ray spectral analysis

In Fig. 4 the total Windowed Timing (WT) 0.3–10 keV spectrum (left panel) and the total Photon Counting (PC) spectrum (right panel) are shown. The adopted model is an absorbed power law. The Galactic absorption is taken into account separately and the intrinsic  $N_{\text{H}}$  is given in the GRB rest frame. All uncertainties are at the 90% cl.

The parameters of the fit for the WT spectrum (119–309 s) are

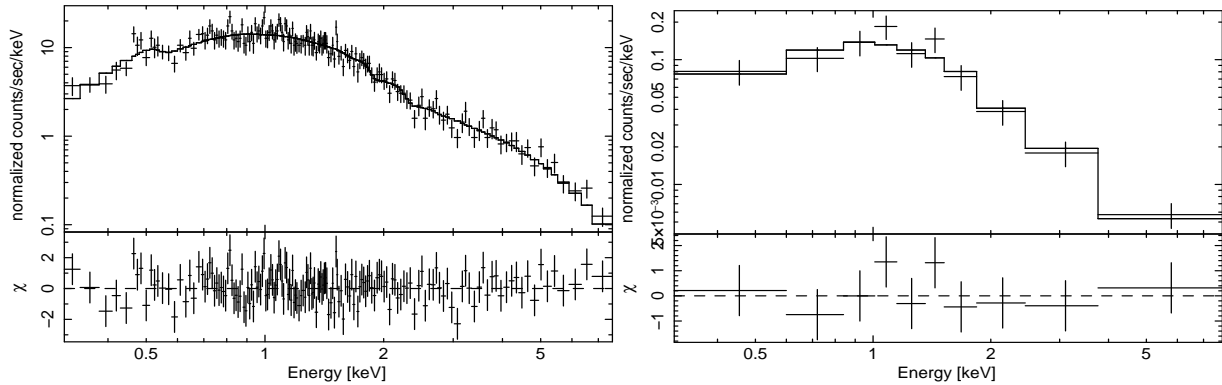


Figure 4. Left panel: XRT WT spectrum. Right panel: XRT PC spectrum.

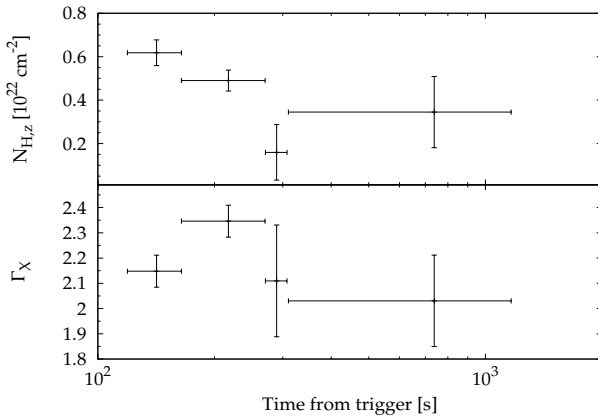


Figure 5. Intrinsic  $N_{\text{H}}$  and photon index as a function of time. Error bars shown are  $1\sigma$ .

$N_{\text{H(Gal)}} = 2.4 \times 10^{20} \text{ cm}^{-2}$  (fixed),  $N_{\text{H,z}} = (5.1 \pm 0.6) \times 10^{21} \text{ cm}^{-2}$ , and  $\Gamma_{\text{X}} = 2.2 \pm 0.1$  ( $\chi^2/\text{dof} = 142/161$ ). The parameters of the fit for the PC spectrum (310–1165 s) are  $N_{\text{H(Gal)}} = 2.4 \times 10^{20} \text{ cm}^{-2}$  (fixed),  $N_{\text{H,z}} = 3.4_{-2.5}^{+3.4} \times 10^{21} \text{ cm}^{-2}$ , and  $\Gamma_{\text{X}} = 2.0 \pm 0.3$  ( $\chi^2/\text{dof} = 4.8/7$ ).

### 3.2.3 X-ray temporally resolved analysis

We extracted the XRT spectra in four separate time intervals each collecting 2000 source photons. In Fig. 5 we plot the  $N_{\text{H}}$  (intrinsic) and the photon index as a function of time. Clearly, as also shown in Fig. 3, there is marginal evidence for a hard-soft-hard trend in the photon index evolution; the same holds for the  $N_{\text{H}}$  evolution.

### 3.3 Combined gamma/X-ray analysis

We calculated the flux in the 0.3–10 keV band after removing the  $N_{\text{H}}$  at low energies, both Galactic and intrinsic. Then we extrapolated it into the BAT 15–150 keV band taking into account the  $\Gamma = 2.2$  unbroken power-law spectrum between XRT and BAT. The result is shown in Fig. 6, in which the initial exponential X-ray decay perfectly matches the decay of the FRED prompt emission seen by BAT. In this case we allowed the peakedness of the Norris profile free to vary. The best-fitting shown is obtained by fitting both fluxes together (90% cl) with  $t_{\text{peak}}^{\text{BAT+XRT}} = 0 \pm 15 \text{ s}$ ,  $t_{\text{rise}}^{\text{BAT+XRT}} = 36_{-24}^{+30} \text{ s}$ ,  $t_{\text{decay}}^{\text{BAT+XRT}} = 147_{-20}^{+17} \text{ s}$ , and peakedness =  $1.64_{-0.16}^{+0.15}$  ( $\chi^2/\text{dof} = 163/128 \approx 1.3$ ). The fit was done on the points earlier than  $t = 400 \text{ s}$ , after

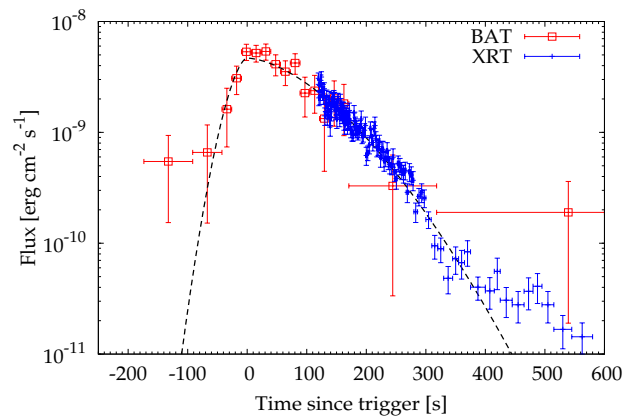


Figure 6. The joint BAT-XRT light curve can be fitted with the same Norris profile used for the BAT emission. See Section 3.3 for details.

which the power law takes over (not shown in this plot). It is clear that the initial steep decay seen in the X-ray band is just the tail of the exponential (single shot) decay observed in the  $\gamma$ -ray band, corresponding to the tail of the prompt emission.

### 3.4 The choice of $t_0$

The decay index of early afterglows is very sensitive to the choice of  $t_0$ . Correctly choosing  $t_0$  is essential to derive the right index as well as to understand the emission process (Piro et al 2005; Tagliferri et al. 2005; Quimby et al. 2006). In the previous section,  $t_0$  is set at the GRB trigger time, and it is almost at the peak of the prompt emission. If the emission is due to an internal shock or external shock,  $t_0$  should be set before the peak (Lazzati & Begelman 2006; Kobayashi & Zhang 2007).

We can see how the choice of  $t_0$  affects the decay index as follows (e.g., Yamazaki 2008). Let  $t$  be the time since the GRB trigger; the peak is located at  $t = 0 \text{ s}$  on this time scale. Next, assuming that the temporal decay right after the peak is actually described by a power law with another time ( $T = t + t_0$ ), where the interval between the time  $T = 0$  and  $t = 0$  is assumed to be exactly  $t_0$ , we get

$$f \propto T^{-\alpha} \propto (t + t_0)^{-\alpha}. \quad (3)$$

Doing this, one finds that the flux  $f$  is constant if  $t \ll t_0$ , while it is described by a power law  $f \propto t^{-\alpha}$  if  $t \gg t_0$ .

Although we have fit the early BAT-XRT data with an expo-

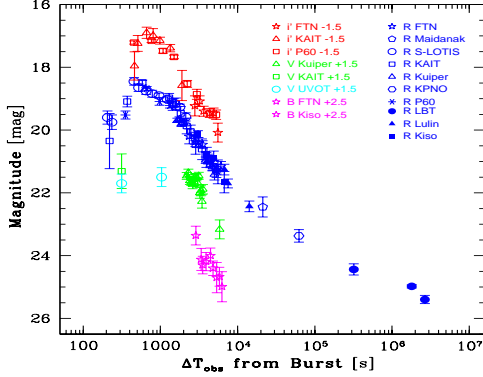


**Figure 7.** Observed optical light curves (*BVRi'*) for the afterglow of GRB 070419A.

nential function, it might be possible to fit the same data by a single power law with a different value of  $t_0$ . We tested this possibility by reexamining the data assuming different values for  $t_0$ . The decay indices right after the peak are  $\alpha = 2.1 \pm 0.13$  if  $t_0 = 100$  s,  $\alpha = 3.2 \pm 0.2$  if  $t_0 = 200$  s, and  $\alpha = 4.2 \pm 0.3$  if  $t_0 = 300$  s.

In all the cases, the light curves still have a clear break around the penultimate BAT point (corresponding to  $T \approx t_0 + 250$  s, for any chosen value of  $t_0$ ). With an even larger  $t_0$ , it is possible to describe the light curve roughly with a single power law. However, the best-fitting value of  $\alpha$  is already very high with  $t_0 = 300$  s and it would be even higher for a larger  $t_0$ . The upper limit on the decay index is given by  $\alpha = 2 + \beta$  (the high-latitude emission), where  $\beta$  is the spectral index. The best-fitting value for  $t_0 = 300$  s ( $\alpha = 4.2 \pm 0.3$ ) is already greater than this upper limit. Furthermore, after the break, the decay is even steeper ( $\alpha = 6.8 \pm 0.8$  or higher for correspondingly larger values of  $t_0$ ). Thus, the post-break index is steeper than the limit from the high-latitude emission.

The early BAT-XRT light curve is described neither by the emission from an external shock nor by that from a single internal shock. The very steep decay between  $t = 250$  s and  $t = 300$  s indicates that the central engine is active at least for  $\sim 250$  s, and that the early part ( $t < 250$  s) should be the result of the superposition of many pulses (internal shocks). Late-afterglow modeling is insensitive to the choice of  $t_0$ . In the rest of the paper (discussion on intermediate/late-time afterglow) we assume  $t_0 = 0$  s.

### 3.5 Optical Light Curve

Fig. 7 shows the optical light curve. Even if the light curve is well sampled only in the *R* band, the general behaviour is seen in all the other optical bands. The top panel of Fig. 8 is a linear-log plot of the  $\gamma$ -ray/X-ray/optical light curves for an immediate comparison with Fig. 6. In the bottom panel of the same figure (log-log scale) it is possible to appreciate how the peak in the optical band coincides with the deviation in the X-ray band from the exponential tail.

In Fig. 9 we show the simple fit of the *R*-band light curve with a series of single power-law segments. Each segment is shown together with the sum of the two components at late times. The value of the decay index of each power law is reported in Table 3, together with the time intervals over which the data has been fitted by the correspondent component. The  $\chi^2/\text{dof}$  of the late-time fit  $f(x)$  (after  $10^3$  s), consisting of the two components  $f_3$  and  $f_4$ , is  $37/41 = 0.91$ .

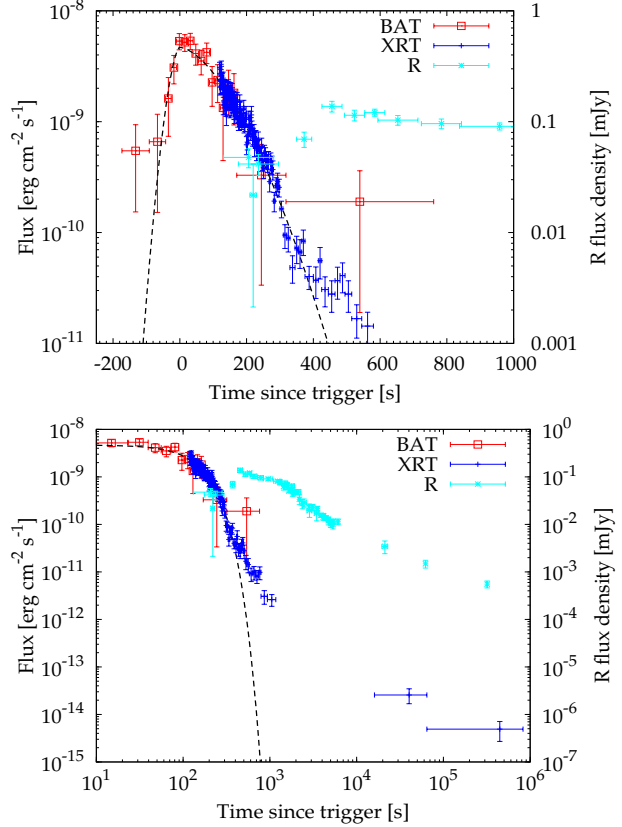


**Figure 8.** *Top panel:*  $\gamma$ -ray/X-ray/optical light curves on a linear-log scale. Same as in Fig. 6 for the joint BAT-XRT light curve. We overplot the optical flux in the *R* band. *Bottom panel:*  $\gamma$ -ray/X-ray/optical light curves on a log-log scale. In this case we excluded from the plot the initial fluxes in the  $\gamma$ -ray (at negative times) and show the late-time optical and X-ray behaviours.

**Table 3.** Best-fitting parameters of the optical light curve.

Component	$N^{\text{opt}}(F_j)$ (mJy)	$\alpha$	$t_{\text{interval}}$ (s)
$f_1$	$(6.84 \pm 2.83) \times 10^{-6}$	$-1.56 \pm 0.70$	$< 460$
$f_2$	$5.81 \pm 3.58$	$0.61 \pm 0.09$	$460 < t < 1500$
$f_3$	$(3.8 \pm 3.2) \times 10^3$	$1.51 \pm 0.12$	$1500 < t < 10^4$
$f_4$	$0.09 \pm 0.19$	$0.41 \pm 0.17$	$t > 10^4$

### 3.6 Infrared data and spectral energy distribution

The fading afterglow of GRB 070419A was detected in the infrared (IR) bands thanks to the United Kingdom Infrared Telescope (UKIRT). Observations started about 40 min after the event and were performed with *JHK* filters (Rol et al. 2007). The calibrated IR magnitudes (with respect to the 2MASS catalogue) are reported in Table 2. As for the optical band, IR magnitudes have been corrected for the estimated extinction ( $A_J = 0.025$  mag,  $A_H = 0.016$  mag,  $A_K = 0.010$  mag) and then converted into flux densities. Coupling those data with optical and X-ray data, we have constructed a spectral energy distribution (SED) extrapolating/interpolating the observations at a common time, chosen to be  $t_{\text{SED}} = 3000$  s = 50 min after the burst. In doing this, we excluded the estimate of the flux in the *V* band, for which the calibration of the optical data is uncertain and therefore the inferred value for the flux density is not

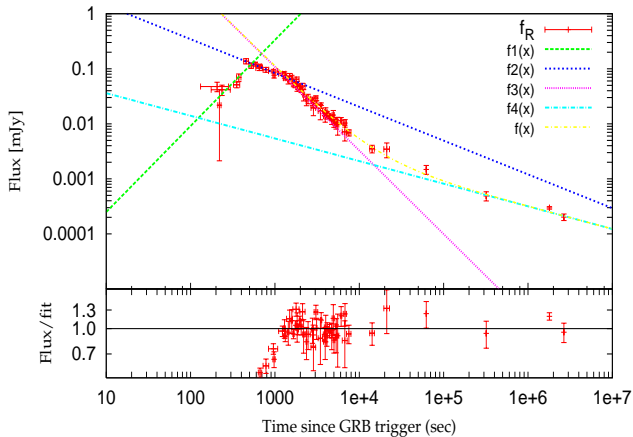


**Figure 9.** *R*-band optical light curve best-fitting. The fit  $f(x)$  is the sum of two power laws ( $f_3$ ,  $f_4$ ) for which the parameters are reported in Table 3. The lower panel shows the residuals of the fit for the last two components.

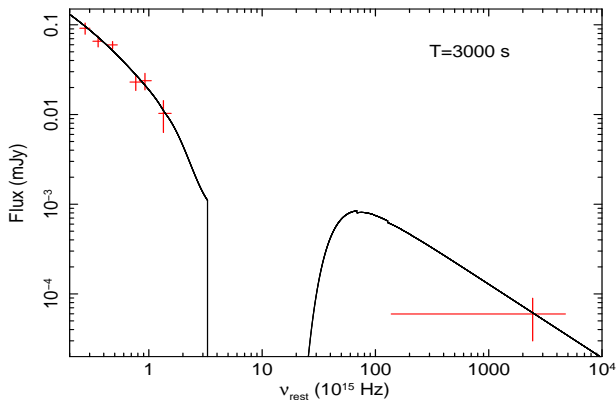


**Figure 10.** Spectral energy distribution fit at  $t = 3000$  s after the burst event.

accurate. The extrapolated fluxes for all the filters are reported in Table 4.

The SED, showed in Fig. 10, is well fitted by a simple optically absorbed power law. The absorption in the X-ray band has been fixed to a negligible value because it cannot be determined by the fit with a single X-ray point. The assumed extinction profile is the Small Magellanic Cloud (SMC) profile (Pei 1992). The best-fitting values in the rest frame of the GRB ( $z = 0.97$ ) are  $\beta_{OX} = 0.82_{-0.07}^{+0.16}$  and  $A_V = 0.37 \pm 0.19$  mag.

## 4 DISCUSSION

### 4.1 X-ray emission

From the analysis of the high-energy data of GRB 070419A it seems clear that the emission can be simply explained by a central engine still active up to at least 250 s, very likely up to  $10^3$  s (see Fig. 2). After that time, the forward-shock emission takes over and the X-ray light curve can be explained by a simple power-law decay (or a slightly complex two-component model).

**Table 4.** Observed  $F_\nu(t = \Delta t)$  and extrapolated  $F_\nu(t = 3000$  s) flux.

Band	$\Delta t$ [s]	$F_\nu(\Delta t)$ [mJy]	$F_\nu(3000$ s) [mJy]
<i>B</i>	2878	$0.0205 \pm 0.0057$	$0.0103 \pm 0.0040$
<i>V</i>	2930	$0.0392 \pm 0.0039$	$0.0306 \pm 0.0040$
<i>R</i>	3063	$0.0292 \pm 0.0029$	$0.0238 \pm 0.0050$
<i>i'</i>	2799	$0.0194 \pm 0.0058$	$0.0230 \pm 0.0045$
<i>J</i>	2930	$0.0614 \pm 0.0051$	$0.0059 \pm 0.0050$
<i>H</i>	2642	$0.0766 \pm 0.0092$	$0.0065 \pm 0.0090$
<i>K</i>	3225	$0.0838 \pm 0.0014$	$0.0916 \pm 0.0014$
X-ray		*	$6.0 \pm 3.0 \times 10^{-5}$

\*Due to the sparse coverage in the X-ray band after  $\sim 10^3$  s, the extrapolation of the X-ray flux at  $t = 3000$  s has been done taking into account the two possible fits for the late-time behaviour as described in Section 3.2.1.

### 4.2 Optical emission

Clearly the optical light curve (Fig. 7) is too complex to be explained with the standard forward shock (FS) model. In general, optical brightening could be due to the enhancement in the ambient density. Since the luminosity above the cooling frequency is insensitive to the ambient density, if the X-ray band is located above the cooling frequency, the lack of a corresponding peak in the X-ray light curve would be naturally explained. However, the features in the optical light curve are too sharp to be explained by the density enhancement model (Nakar & Granot 2007). Another mechanism should be responsible for the production of the observed optical features.

A possible mechanism is reverse shock (RS) emission which dominates in the optical band at early times. Although the decay behaviour of  $\sim t^{-2}$  is well known for the RS emission, the initial decay could be as shallow as  $t^{-0.5}$  if the typical frequency is above the optical band ( $\nu_{\text{opt}} < \nu_{m,r} < \nu_{c,r}$ ) at the RS crossing time (Sari & Piran 1999; Kobayashi 2000). Since the observed index ( $\alpha = 0.61 \pm 0.09$ ) is consistent with the expected value, we test this possibility in detail.

Assuming that the optical peak ( $t_{\text{peak}} \approx 450$  s) gives the fireball deceleration time, we can estimate the initial Lorentz factor of the fireball as  $\Gamma \approx 350n^{-1/8}((1+z)/1.97)^{3/8}(T/450 \text{ s})^{-3/8}(E/(2 \times 10^{51} \text{ erg}))^{1/8}$ . If the break in the optical light curve around 1500 s is due to the passage of the typical frequency of the RS,  $\nu_{m,r} \propto t^{-54/35}$ , through the optical band (Kobayashi 2000),  $\nu_{m,r}$  should be around  $3 \times 10^{15}$  Hz at  $t = t_{\text{peak}}$ . The typical frequency of the FS,  $\nu_{m,f} = \Gamma^2 \nu_{m,r}$ , should be about  $4 \times 10^{20}$  Hz at the peak time (e.g., Kobayashi & Zhang 2003). We expect that the FS emission in the optical band should increase as  $t^{1/2}$  in the ISM (or  $t^{-1/4}$  in the wind ambient) until  $t \approx 4 \times 10^6$  s when  $\nu_{m,f} \propto t^{-3/2}$  passes through the optical band. Since the observed optical luminosity already decreases as  $t^{-0.4}$  or steeper around  $10^4$  s, this is not consistent.

If the fireball is magnetized, the  $\nu_{m,f}$  could be smaller by a factor of  $R_B^{-1/2}$ , where  $R_B$  is the ratio of the microscopic parameters in the two shock regions (we use the same notation as Gomboc et al. 2008;  $R_B = \varepsilon_{B,r}/\varepsilon_{B,f}$ ). The passage time of  $\nu_{m,f}$  through the optical band scales as  $R_B^{1/3}$ . In order to get a FS peak time two orders of magnitude smaller, a very large  $R_B \approx 10^6$  is needed. With this value of  $R_B$ , the luminosity ratio between the RS and FS peaks is about  $\Gamma R_B^{1/2} \approx 4 \times 10^5$ . In the observational data, the RS component is only a few times brighter than the FS component. The introduction of magnetization cannot fix the problem with the FS

peak. If we stick with the RS model, the typical frequency of the RS emission ( $\nu_{m,r}$ ) should be well below the optical band at the shock crossing time. The initial shallow decay ( $t^{-0.5}$ ) in the optical might be explained with energy injection to the fireball ejecta (refreshed shocks). We cannot rule out this possibility, but the energy injection rate should be tuned very carefully in order to reproduce the observed power-law decay, and moreover we would need to assume a sharp cessation of the injection to get the clear break.

The shallow decay phase observed between 450 and 1500 s, still described by a power-law, and the very sharp transitions from one power-law to another in the optical light curve are puzzling features for any model. One possible explanation of the observed features in the optical light curve is the assumption of a finely tuned long-lived central engine. This condition is indeed necessary to explain the plateau phase observed in the canonical X-ray light curves of many GRBs.

### 4.3 Supernova/host-galaxy contribution

As discussed above, the optical light curve continues to decay to late times with an unusually shallow gradient. Late-time observations consist of LBT detections in the SDSS-*r* filter, the first ( $t \approx 3.2 \times 10^5$  s) and third ( $t \approx 2.6 \times 10^6$  s) of which are consistent with the shallow decay of the afterglow emission. At  $t \approx 1.8 \times 10^6$  s, a small excess above the underlying power law is observed (see Fig. 7). This feature has been attributed to a possible supernova component (Dai et al. 2008), but interpretation of the late-time data are critically dependent on the model of the underlying afterglow. Given the faintness of the emission at these late times ( $r' \approx 25.7$  mag), which is not atypical for GRB host-galaxy magnitudes at this redshift (Wainwright et al. 2007; Ovaldsen et al. 2007), future deep optical imaging of the GRB location would confirm whether a host-galaxy contribution is present or the light has continued to decline below detection limits.

## 5 CONCLUSIONS

- The  $\gamma$ -ray profile of GRB 070419A consists of a single shot (FRED) a few hundred seconds long. The  $\gamma$ -ray fluence ( $\sim 5 \times 10^{-7}$  erg cm $^{-2}$ ) has an average value for the *Swift* GRB population, but the peak photon flux puts this event at the low end of that distribution among *Swift* GRBs (Sakamoto et al. 2008).

- The XRT 0.3–10 keV data show the presence of some intrinsic (rest-frame) absorption, and there is weak evidence for an evolution of both  $N_H$  and the photon index (mean value of  $\Gamma_X \sim 2.2$ ) with time.

- The XRT-BAT fluxes, derived in the 15–150 keV band after removing the absorption in XRT curves, shows that the initial steep X-ray decay is just the decay of the FRED, modelled with a Norris profile (Norris et al. 1996). The early BAT-XRT light curve is due to internal shocks or other processes related to prolonged central engine activity up to at least 250 s.

- After 400–500 s, the late-time X-ray power law begins to emerge, with index  $\alpha_X \approx 1.2 \pm 0.2$  (or  $\alpha_{X,2} \approx 0.7$  in the case of the more complex fit model with two power laws). This behaviour seems to be supported by the optical light curve that shows a peak roughly at the same time ( $t_{\text{peak}} \approx 450$  s).

- We tried to explain the behaviour of the optical light curve in the context of the standard fireball model. However the simple and natural explanation (FS plus RS components) does not work. The

magnetization of the ejecta could affect the FS peak time significantly, but the effect is negligible and not in agreement with the observations. Another possibility to explain the optical behaviour is to argue for the existence of a significant density enhancement in the ambient medium. The luminosity below the cooling frequency is proportional to  $\rho^{1/2}$ . If a blast wave hits a density enhancement of several tens or hundreds, the bump in the optical at  $\sim 450$  s could be explained. However, the observed peak feature might be too sharp for this model.

- We cannot rule out the possibility of a finely tuned central engine for GRB 070419A. However, the optical light curve would not be easily reproduced without assuming a particular energy injection rate and a sudden cessation of the injection in order to create the observed optical features.

- From our detailed multiwavelength analysis we can conclude that GRB 070419A is not explained in the context of the simple standard fireball model. Assuming energy injection or a tail component following the fireball, or even a more complex emission picture, the RS model might explain the observations, but this scenario would result in a rather *ad hoc* explanation only for this particular event.

## ACKNOWLEDGMENTS

AM acknowledges funding from the Particle Physics and Astronomy Research Council (PPARC). CGM is grateful for financial support from the Royal Society and Research Councils UK. AVF's group is supported by US National Science Foundation (NSF) grant AST-0607485, Gary and Cynthia Bengier, and the TABASGO Foundation. The Liverpool Telescope is operated by Liverpool John Moores University at the Observatorio del Roque de los Muchachos of the Instituto de Astrofísica de Canarias. The Faulkes Telescopes, now owned by Las Cumbres Observatory, are operated with support from the Dill Faulkes Educational Trust. KAIT and its ongoing operation were made possible by donations from Sun Microsystems, Inc., the Hewlett-Packard Company, AutoScope Corporation, Lick Observatory, the NSF, the University of California, the Sylvia & Jim Katzman Foundation, and the TABASGO Foundation. We thank R. Chornock for initial discussions of the KAIT data on the optical afterglow of GRB 070419A. This work made use of data supplied by the UK *Swift* Science Data Centre at the University of Leicester.

## REFERENCES

- Barthelmy, S. D., et al. 2005, *Space Science Reviews*, 120, 143  
 Burrows, D. N., et al. 2005, *Science*, 309, 1833  
 Cenko, S. B., et al. 2007, *GCN Circ.* 6322  
 Cenko, S. B., et al. 2008, *ApJ*, submitted (arXiv:0808.3983)  
 Chincarini, G., et al. 2007, *ApJ*, 671, 1903  
 Chornock, R., et al. 2007, *GCN Circ.* 6304  
 Cool, J., et al. 2007, *GCN Circ.* 6318  
 Dai, X., et al. 2008, *ApJ*, 682, L77  
 Falcone, A. D., et al. 2007, *ApJ*, 671, 1921  
 Fukugita, M., et al. 1996, *AJ*, 111, 1748  
 Kobayashi, S., & Zhang, B. 2003, *ApJ*, 582, L75  
 Kobayashi, S., & Zhang, B. 2007, *ApJ*, 655, 973  
 Krimm, H. A., et al. 2004, *AIP Conf. Proc.*, 727, 659  
 Lazzati, D., & Begelman, M. C. 2006, *ApJ*, 641, 972  
 Melandri, A., et al. 2008, *ApJ*, 686, 1209



- Norris, J. P., et al. 1996, *ApJ*, 459, 393  
Nousek, J. A., et al. 2006, *ApJ*, 642, 389  
O'Brien, P. T., et al. 2006, *ApJ*, 647, 1213  
Panaitescu, A., & Kumar, P. 2004, *MNRAS*, 353, 511  
Pei, Y. C. 1992, *ApJ*, 395, 130  
Perri, M., et al. 2007, *GCN Circ.* 6333  
Piro, L., et al. 2005, *ApJ*, 623, 314  
Quimby, R. M., et al. 2006, *ApJ*, 640, 402  
Rees, M. J., & Mészáros, P. 1992, *MNRAS*, 258, 41  
Rol, E., et al. 2007, *GCN Circ.* 6309  
Roming, P. W. A., et al. 2005, *Space Science Reviews*, 120, 95  
Sakamoto, T., et al. 2008, *ApJS*, 175, 179  
Schlegel, D., et al. 1998, *ApJ*, 500, 525  
Stamatikos, M., et al. 2007a, *GCN Circ.* 6302  
Stamatikos, M., et al. 2007b, *GCN Circ.* 6326  
Stamatikos, M., et al. 2007c, *GCN Report* 47.1  
Tagliaferri, G., et al. 2005, *Nature*, 436, 985  
Yamazaki, R. 2009, *ApJ*, 690, 118  
Zhang, B., Kobayashi, S., & Meszaros, P. 2003, *ApJ*, 595, 950  
Zhang, B., et al. 2006, *ApJ*, 642, 354